

ResGS: Residual Densification of 3D Gaussian for Efficient Detail Recovery

Yanzhe Lyu Kai Cheng Xin Kang Xuejin Chen[†]
 MoE Key Laboratory of Brain-inspired Intelligent Perception and Cognition
 University of Science and Technology of China

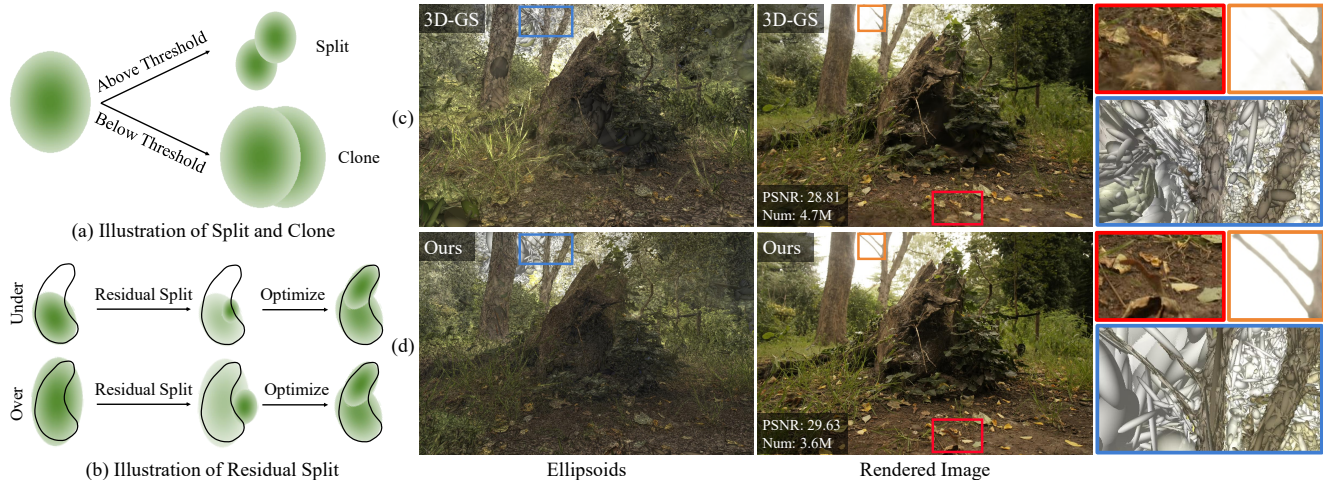


Figure 1. We propose ResGS, a pipeline to boost the rendering quality of 3D-GS [23] while improving efficiency. (a) The 3D-GS densification operations, split and clone, rely on binary selection and cannot adaptively address the challenges they encounter. (b) Our ResGS employs a single densification operation, residual split, that adaptively addresses under-reconstruction and over-reconstruction. (c) 3D-GS tends to generate Gaussians with sizes in small variation and low rendering quality. (d) From the same initialization, our method can capture fine details and retrieve sufficient geometry effectively while reducing redundancy.

Abstract

Recently, 3D Gaussian Splatting (3D-GS) has prevailed in novel view synthesis, achieving high fidelity and efficiency. However, it often struggles to capture rich details and complete geometry. Our analysis reveals that the 3D-GS densification operation lacks adaptiveness and faces a dilemma between geometry coverage and detail recovery. To address this, we introduce a novel densification operation, **residual split**, which adds a down-scaled Gaussian as a residual. Our approach is capable of adaptively retrieving details and complementing missing geometry. To further support this method, we propose a pipeline named ResGS. Specifically, we integrate a Gaussian image pyramid for progressive supervision and implement a selection scheme that prioritizes the densification of coarse Gaussians over time. Extensive experiments demonstrate that our method achieves SOTA rendering quality. Consistent performance improvements can

be achieved by applying our residual split on various 3D-GS variants, underscoring its versatility and potential for broader application in 3D-GS-based applications. Project page: <https://yanzhelyu.github.io/resgs.github.io/>.

1. Introduction

Novel View Synthesis (NVS) has continued to be a hot topic throughout the years. Traditional methods like point clouds and meshes [4, 9, 13] can achieve high rendering speed but often lack fidelity. On the other hand, neural volumetric approaches [1, 29, 30] can achieve high fidelity for novel views but significantly sacrifice rendering efficiency. Recently, 3D-GS [23] has shown both high fidelity and fast rendering speed for novel view synthesis. However, 3D-GS still suffers from setbacks, often failing to capture fine details or recover complete geometry, as shown by the red and orange rectangles in Fig. 1 and Fig. 2.

While various approaches [12, 43, 48, 50] have been proposed to tackle these challenges and have significantly ad-

[†]Corresponding author.

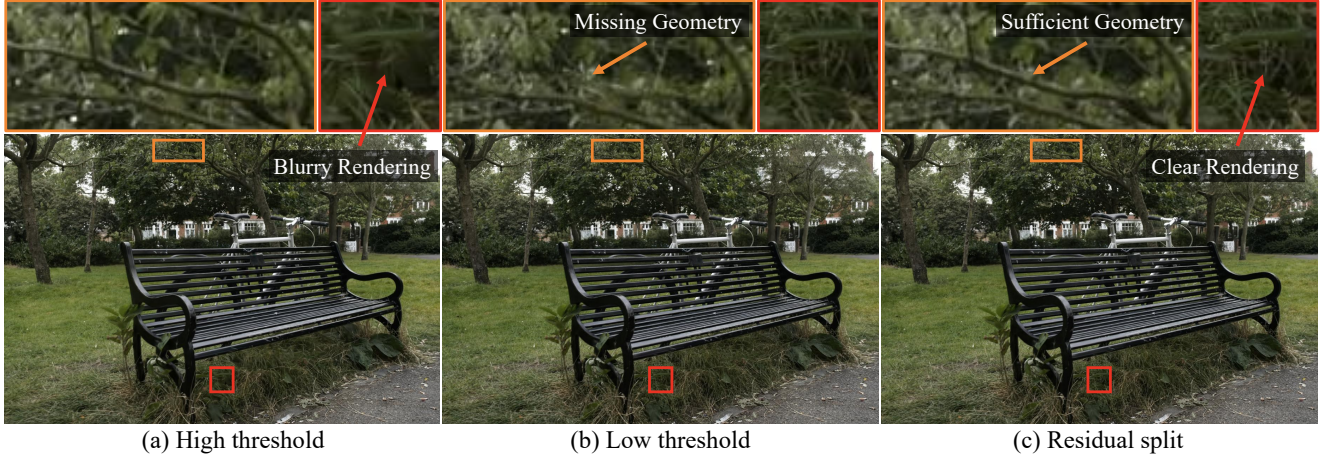


Figure 2. **An illustration of the limitation of split and clone.** (a) selects between split and clone based on a high threshold, (b) a low threshold, and in (c) the densification operation is replaced as residual split. We provide visualizations of the final rendered image. A high threshold ensures sufficient structural coverage but causes over-reconstruction, leading to blurry rendering. Conversely, a low threshold mitigates blurry rendering but results in under-reconstruction, compromising coverage and creating a difficult trade-off. Our method, however, adaptively tackles both issues without facing this trade-off.

vanced the rendering quality of 3D-GS-based methods to state-of-the-art (SOTA) levels, they seldom adapt the densification operation of 3D-GS. In this paper, we go through the densification procedure and propose a novel adaptive densification approach to improve reconstruction quality.

The densification operation used in 3D-GS-based methods consists of two operations: split and clone. The split operation is designed to address over-reconstruction, where a single Gaussian covers too much area, and the clone operation aims to compensate for under-reconstruction. However, selecting between the two operations properly in different areas is challenging and existing methods rely on a threshold-based decision mechanism. As illustrated in Fig. 1 (a), Gaussians whose scale $s = \max(s_x, s_y, s_z)$ is larger than a predefined threshold τ_s undergo split, while those below it use clone. The simplicity of this threshold-based densification usually leads to suboptimal results and encounters a dilemma in threshold selection. As highlighted by the red rectangles in Fig. 2 (a), a high threshold results in insufficient split preventing the model from capturing fine details and leading to blurry rendering. On the other hand, a low threshold suppresses clone operations, leading to missing geometry, as illustrated in the orange boxes in Fig. 2 (b). Furthermore, 3D-GS tends to first split and then clone, resulting in objects being fitted with Gaussians of similar scales. As highlighted by the blue rectangles in Fig. 1, 3D-GS fits textureless areas with an excessive number of small Gaussians, which is redundant.

To tackle the aforementioned problems, we propose **residual split**, a novel densification operation in 3D Gaussian splatting. As illustrated in Fig. 1 (b), the core idea is to spawn a downscaled replica as a residual component while

reducing the original Gaussian’s opacity for any under-optimized Gaussian. This simultaneously expands spatial coverage and injects finer details, eliminating the dilemma of selecting split or clone.

However, directly applying residual split does not produce significant improvements. This is due to the inefficiency the 3D-GS initialization. At early iterations, the scene is represented by a few coarse Gaussians that very likely face both over-reconstruction and under-reconstruction. Gaussians added through densification are challenging to optimize, as they must address both issues simultaneously. It’s desired to develop an approach that decouples coverage and detail optimization.

Correspondingly, we propose a coarse-to-fine training pipeline, **ResGS**, that progressively shifts the focus of training, facilitating optimization. Firstly, we structure the training process into stages, employing multi-scale images for gradual supervision, ensuring that the early stages focus on the overall structure and the later stages focus on details. Secondly, we develop a progressive Gaussian selection scheme for densification, which gradually encourages coarser Gaussians to undergo further refinement. Therefore, finer structures are introduced at later iterations, avoiding premature optimization. These two techniques simplify optimization and thereby improve rendering quality.

Our contributions are summarized as follows:

- We propose a novel densification operation for 3D Gaussians based on a residual strategy to overcome the limitations of fixed threshold for determining split or clone in 3D-GS;
- We develop a coarse-to-fine training pipeline, ResGS. Equipped with the proposed residual split, it incorpo-

rates a multi-scale supervision with image pyramids and a Gaussian selection scheme to enhance rendering quality;

- Our method achieves SOTA rendering quality in NVS on three datasets, including Mip-NeRF360 [1], Tanks&Temples [24], and DeepBlending [17]. Furthermore, applying our proposed residual split to multiple 3D-GS variants consistently brings performance improvements, demonstrating that our new densification operation is more effective than densification with a fixed scale threshold.

2. Related Work

2.1. Novel View Synthesis

Novel view synthesis (NVS) aims to acquire novel view images for a scene through a set of multi-view images. As a pioneer, NeRF [29] introduced an MLP-based implicit representation. More specifically, it uses an MLP to predict the color and opacity of a point in a scene and uses differentiable volume rendering to render images. Due to its photo-realistic quality, it has been extensively studied [1, 2, 6–8, 21, 26, 47]. However, NeRF-based methods often suffer from long training and rendering time. Therefore, many works [18, 19, 31, 32] have been proposed to extend NeRF into real-time rendering.

Recently, 3D-GS [23] has stirred an evolution in the field by achieving both high-fidelity and real-time rendering. Due to its high performance, many works have enabled 3D-GS into many downstream tasks such as SLAM [28, 41], 3D generation [10, 37, 44, 52], 4D scene modeling [15, 25, 39, 42], and surface reconstruction [14, 20].

However, the original 3D-GS still has limitations, and myriad works have been proposed to increase the render quality and efficiency of 3D-GS. Mip-Splatting [46] introduced a 2D dilation filter and a 3D smoothing filter to mitigate aliasing and artifacts caused by changes in focal length. Scaffold-GS [27] proposed the concept of neural Gaussians which is to tie Gaussians around an anchor and use an MLP to predict its attributes. Thus, the model is more robust to significant view changes and can improve rendering quality. AbsGS [43] discovered that when accumulating the view space gradients used in densification through pixels, there could be a collision, for gradients at various pixels might have different positivities. They applied an absolute function before summing through pixels to mitigate the issue. Pixel-GS [50] analyzed 3D-GS artifacts from the pixel perspective and introduced a method to select Gaussians for densification based on this analysis. GaussianPro [11] introduced a progressive propagation strategy to propagate Gaussians to under-initialized areas. To reduce redundancy and increase rendering quality, Mini-Splatting [12] proposed a densification and simplification algorithm to reorganize Gaussians’ spatial positions.

With the emergence of numerous works focused on optimizing NeRF and 3D-GS, progressive training schedules—proven effective in multiple scenarios [3, 16, 22, 34] have earned attention.

2.2. Progressive Training in NVS

Several progressive training schedules have been explored upon NeRF-based methods. BungeeNeRF [40] captured different levels of details in large city-scale datasets by gradually adding closer views to the training views and appending residual blocks to the MLP throughout the training process. Pyramid NeRF [51] employs a coarse-to-fine strategy, using an image pyramid to progressively introduce high-frequency details while simultaneously subdividing the scene representation.

Recently, with the prevalence of 3D-GS, many progressive training pipelines have been proposed. Octree-GS [33] proposed an Octree-based 3D-GS approach, and the Octree depth is progressively deepened. FreGS [48] designed a progressive frequency regulation for 3D-GS which is to calculate the loss of rendered images in the frequency domain and gradually add higher frequency components.

3. Our Method

3.1. Preliminaries

3D Gaussian Splatting. The 3D-GS work [23] represents a 3D scene with a set of anisotropic 3D Gaussians for fast and high-quality rendering. Each Gaussian primitive consists of two parameters, mean μ and covariance matrix Σ , representing its position and shape:

$$G(\mathbf{x}) = e^{-\frac{1}{2}(\mathbf{x}-\mu)^T \Sigma^{-1}(\mathbf{x}-\mu)}. \quad (1)$$

To model the positive semi-definite property of the covariance matrix Σ , a scaling matrix \mathbf{S} and a rotation matrix \mathbf{R} is used as:

$$\Sigma = \mathbf{R} \mathbf{S} \mathbf{S}^T \mathbf{R}^T, \quad (2)$$

where a 3D vector $\mathbf{s} = (s_x, s_y, s_y)$ is used for the scaling matrix \mathbf{S} .

Furthermore, each Gaussian also contains a spherical harmonics coefficients SH and opacity o . In rendering, tile-based rasterization is applied: 3D Gaussians $G(\mathbf{x})$ are projected as 2D Gaussians $G'(\mathbf{x})$ on the image plane. A view-dependent color c is then derived from SH , and the 2D Gaussians are sorted by depth and rendered using alpha-blending:

$$C(\mathbf{x}) = \sum_{i \in N_{\mathbf{x}}} c_i \alpha_i(\mathbf{x}) \prod_{j=1}^{i-1} (1 - \alpha_j(\mathbf{x})), \quad (3)$$

$$\alpha_i(\mathbf{x}) = c_i G'_i(\mathbf{x}),$$

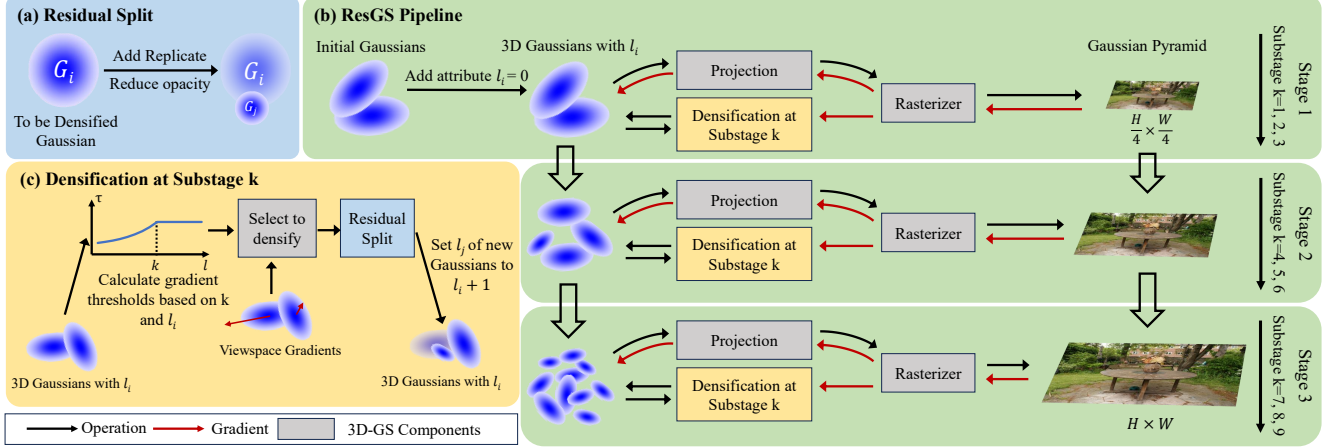


Figure 3. **Overview of our ResGS pipeline.** (a) The core of our pipeline, residual split, involves adding a downscaled replicate and then reducing the opacity of the original Gaussian. (b) We assign initial Gaussians a temporary attribute $l_i = 0$ for densification selection, which is discarded after training. Next, the pipeline is split into L stages, with each stage trained on images downscaled using an image pyramid. Each single stage is further divided evenly into K substages, for selecting Gaussians to densify. (c) The points selected for densification are determined by the substage k , l_i , and view-space gradients of Gaussians. Residual split is performed upon selected Gaussians, and l_j would be assigned to new Gaussians.

where \mathbf{x} is a pixel position in the rendered image, $C(\mathbf{x})$ the color of the pixel, and $N_{\mathbf{x}}$ the number of Gaussians that covers \mathbf{x} .

During the training process, 3D Gaussians are periodically densified. 3D-GS calculates the average view-space gradients ΔL_i over a certain number (e.g. 100) of iterations to determine whether to perform densification. If ΔL_i exceeds threshold τ , a split or clone action is triggered. The split operation addresses over-reconstruction, where excessive space is covered, while clone addresses under-reconstruction, where additional spatial coverage is needed. To determine whether to split or clone, 3D-GS [23] sets a threshold $\tau_s = kR$, where k is a predefined factor and R is the scene extent. Split occurs when the scale $s = \max(s_x, s_y, s_z)$ of a Gaussian surpasses the threshold τ_s . Clone is applied when $s < \tau_s$.

3.2. ResGS

We propose ResGS, a coarse-to-fine pipeline to boost the rendering quality of 3D-GS with a novel residual densification operation. Fig. 3 shows the overview of our method. We propose a novel densification operation, residual split, (Sec. 3.2.1), to tackle the limitations of the 3D-GS densification operation. Furthermore, we introduce a split-stage supervision schedule to add information to the scene gradually (Sec. 3.2.2). We also design a Gaussian selection scheme that progressively encourages densification for coarse Gaussians to enhance details, as described in Sec. 3.2.3.

3.2.1. Residual Split

The core idea of our densification operation is to generate downscaled Gaussians as residuals to supplement those requiring densification. The newly added Gaussian adaptively enhances the reconstructed model, allowing the scene to be refined as needed. The method is named as residual split. As illustrated in Fig. 3 (a), for a to-be-densified Gaussian G_i , our densification operation consists of two steps. Firstly, we add a down-scaled replicate G_j . Specifically, its opacity o_j , rotation \mathbf{R}_j , spherical harmonics coefficients SH_j would be same as G_i , μ_j is sampled using the original 3D Gaussian as a PDF for sampling, and \mathbf{S}_j is defined as \mathbf{S}_i divided by a predefined factor λ_s :

$$\begin{aligned} \mathbf{S}_j &= \frac{1}{\lambda_s} \mathbf{S}_i, \\ \mathbf{R}_j &= \mathbf{R}_i, SH_j = SH_i, o_j = o_i, \\ \mu_j &\sim \mathcal{N}(\mu_i, \Sigma_i), \end{aligned} \quad (4)$$

where Σ_i is the covariance matrix of G_i . Then, to tackle the density increase in the overlap of the two Gaussians, we reduce the opacity of the original Gaussian. This is accomplished by multiplying its opacity by a predefined factor β :

$$o'_i = \beta o_i. \quad (5)$$

While the clone and split in the original 3D-GS pipeline lack adaptiveness, our residual split can fill in missing geometry and recover details adaptively without requiring a trade-off, as shown in Fig. 2 (c). We further illustrate this using intermediate results, as shown in Fig. 4. In areas where details are challenging to recover, down-scaled

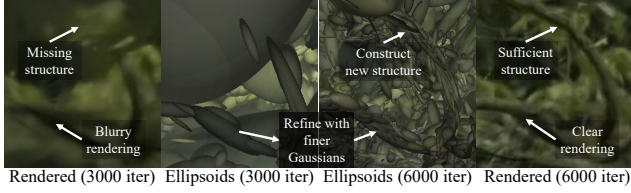


Figure 4. **Intermediate results after applying residual split.** We saved the Gaussians at 3,000 and 6,000 iterations after applying residual split. As observed, residual split can adaptively handle over-reconstruction and under-reconstruction by refining blurry regions with finer Gaussians while also effectively reconstructing missing structures.

Gaussians of finer granularity are progressively introduced to refine and reveal intricate details. On the other hand, since densification does not change the scale of the original Gaussian, the total coverage is increased after densification, helping to reconstruct missing structures. Moreover, our method’s approach to generate nonidentical Gaussians of varying scales enables efficient shape fitting. As illustrated by the blue rectangles in Fig. 1, this non-identicalness allows us to fill textureless regions with a few large Gaussians, significantly reducing redundancy. Consequently, our approach delivers higher rendering quality while using fewer Gaussians.

3.2.2. Image Pyramid as Supervision

To decouple coverage and detail optimization, we design a coarse-to-fine supervision schedule to gradually integrate fine high-frequency information into the scene. Specifically, based on the original multi-view training pictures, we build an image pyramid $\{\mathcal{I}_i\}_{i=1}^L$ consisting of L layers. \mathcal{I}_i corresponds to the set of images at different viewpoints in layer i . \mathcal{I}_L is the set of original pictures:

$$\mathcal{I}_i = \{P_i^v\}_{v \in V}, \quad (6)$$

where V is the set of viewpoints and P_i^v refers to the image at viewpoint v in the i^{th} layer. Let (H_L^v, W_L^v) be the resolution of P_L^v , and (H_i^v, W_i^v) represent the resolution of P_i^v . Then there is:

$$(H_i^v, W_i^v) = (H_L^v/2^{L-i}, W_L^v/2^{L-i}). \quad (7)$$

Correspondingly, our training process is divided into L stages. At the i -th stage, the Gaussians are trained under the supervision of \mathcal{I}_i . At the initial stage with lower image resolution, the 3D Gaussians are optimized to construct an overall structure of the whole scene from coarse and low-frequency features. As the image resolution increases, high-frequency details of the scene gradually emerge, shifting the focus toward adding finer, more intricate features.

3.2.3. Varying Gradient Threshold

To further emphasize the progressive training, we modify the strategy for selecting Gaussians to densify. As the training proceeds, the training focus is desired to shift toward finer details. Thus, we encourage the densification of coarse Gaussians to capture more detail over time. In our residual split, the generated Gaussians are finer than the original ones. Thus, we can track the relative fineness level of each Gaussian G_i , denoted as l_i . We assign l_i of all initial Gaussians to 0. If the level of the Gaussian being densified is l_i , we assign the newly added Gaussian a level of $l_i + 1$. Thus, as l_i gets higher, Gaussians tend to be smaller and finer. Note that l_i is only utilized during rendering and discarded after training.

A single stage is then divided evenly into K substages, creating $L \times K$ substages in total. The gradually increasing substage can be seen as an indicator of the scene details level. At substage k , we promote additional densification for Gaussians with $l_i < k$ and prioritize those at lower levels, achieved by applying varying gradient thresholds. Specifically, the threshold $\tau_{k,i}$ for deciding whether densification is needed for a Gaussian G_i is set as:

$$\tau_{k,i} = \begin{cases} \tau, & l_i \geq k, \\ \frac{\tau}{\alpha^{k-l_i}}, & l_i < k, \end{cases} \quad (8)$$

where τ and $\alpha > 1$ are predefined values.

4. Experiments and Results

4.1. Experimental Settings

Following previous works [12, 23, 27, 33, 43, 48], evaluation of our model was done on three datasets, including all nine scenes from Mip-NeRF360 [1], two scenes from Tanks&Temples [24], and two scenes from Deep Blending [17]. The test and train splits follow those of the original 3D-GS [23], and the image resolution is also maintained as in 3D-GS. Three commonly used metrics were used to quantify the fidelity of rendered images: PSNR, SSIM [38], and LPIPS [49]. We also report the memory consumption as an indicator of the number of Gaussians.

We trained three versions of our model: two with AbsGS [43], leveraging its enhanced indication of Gaussians for densification—one standard version and one small version with higher gradient thresholds—and a third version using 3D-GS as the baseline. We applied the periodic opacity reduction from AbsGS across all three versions, as it proved to be a more effective alternative to the opacity reset used in 3D-GS. Additionally, we extended this reduction beyond the densification phase, finding it further minimized redundancy without compromising fidelity. Following previous methods, we trained our model for 30k iterations. The densification stops at 12000 iterations. For the version with

Table 1. **Quantitative comparison to previous methods on real-world datasets.** Our method achieves SOTA in the Mip-NeRF360 dataset and comparable results with SOTA on the Tanks&Temples and Deep Blending datasets. * indicates results generated by retrained models for different rendering resolution.

| Dataset Method Metrics | Mip-NeRF360 | | | | Tanks&Temples | | | | Deep Blending | | | |
|-----------------------------|-----------------|-----------------|--------------------|--------|-----------------|-----------------|--------------------|--------|-----------------|-----------------|--------------------|--------|
| | PSNR \uparrow | SSIM \uparrow | LPIPS \downarrow | Mem. | PSNR \uparrow | SSIM \uparrow | LPIPS \downarrow | Mem. | PSNR \uparrow | SSIM \uparrow | LPIPS \downarrow | Mem. |
| Plenoxels | 23.08 | 0.626 | 0.463 | 2.1GB | 21.08 | 0.719 | 0.379 | 2.3GB | 23.06 | 0.795 | 0.510 | 2.7GB |
| Instant-NGP | 25.59 | 0.699 | 0.331 | 48MB | 21.92 | 0.745 | 0.305 | 48MB | 24.96 | 0.817 | 0.390 | 48MB |
| Mip-NeRF360 | 27.69 | 0.792 | 0.237 | 8.6MB | 22.22 | 0.759 | 0.257 | 8.6MB | 29.40 | 0.901 | 0.245 | 8.6MB |
| Scaffold-GS* | 27.69 | 0.812 | 0.225 | 176MB | 23.96 | 0.853 | 0.177 | 87MB | 30.21 | 0.906 | 0.254 | 66MB |
| Octree-GS* | 27.52 | 0.812 | 0.218 | 124MB | 24.52 | 0.866 | 0.153 | 84MB | 30.41 | 0.913 | 0.238 | 93MB |
| 3D-GS | 27.21 | 0.815 | 0.214 | 734MB | 23.14 | 0.841 | 0.183 | 411MB | 29.41 | 0.903 | 0.243 | 676MB |
| AbsGS | 27.49 | 0.820 | 0.191 | 728MB | 23.73 | 0.853 | 0.162 | 304MB | 29.67 | 0.902 | 0.236 | 444MB |
| Pixel-GS* | 27.52 | 0.822 | 0.191 | 1.32GB | 23.78 | 0.853 | 0.151 | 1.06GB | 28.91 | 0.892 | 0.250 | 1.09GB |
| FreGS | 27.85 | 0.826 | 0.209 | - | 23.96 | 0.849 | 0.178 | - | 29.93 | 0.904 | 0.240 | - |
| Mini-Splatting-D | 27.51 | 0.831 | 0.176 | 1.11GB | 23.23 | 0.853 | 0.140 | 1.01GB | 29.88 | 0.906 | 0.211 | 1.09GB |
| Ours-Small (AbsGS) | 27.94 | 0.830 | 0.191 | 342MB | 24.33 | 0.862 | 0.150 | 187MB | 30.01 | 0.906 | 0.234 | 289MB |
| Ours (3D-GS) | 28.00 | 0.831 | 0.187 | 600MB | 24.26 | 0.865 | 0.141 | 354MB | 29.93 | 0.903 | 0.232 | 596MB |
| Ours (AbsGS) | 28.00 | 0.833 | 0.174 | 698MB | 24.38 | 0.867 | 0.132 | 351MB | 29.91 | 0.902 | 0.227 | 586MB |

AbsGS, $\tau = 0.00067$, and 0.0016 for the small version. For the version with 3D-GS, $\tau = 0.00028$. We set $L = 3$ and $K = 3$. Our first stage lasts for 2500 iterations, the second stage for 3500 iterations, and the rest iterations are in the last stage. $\alpha = 2^{\frac{1}{3}}$, $\lambda_s = 1.6$ and $\beta = 0.3$. The loss function remains the same as in 3D-GS [23], consisting of a combination of \mathcal{L}_1 and D-SSIM losses. All experiments were done on an NVIDIA RTX3090 GPU.

4.2. Comparisons

To assess the effectiveness of our method, we compare it with several 3D-GS variants: 3D-GS [23], Scaffold-GS [27], Octree-GS [33], FreGS [48], AbsGS [43], Pixel-GS [50] and Mini-Splatting-D [12]. Note that Scaffold-GS and Octree-GS use a latent representation rather than the original 3D-GS representation. Some radiance-field-based methods are also selected for comparison, including Plenoxels [45], Instant-NGP [30] and Mip-NeRF360 [1]. We find that the resolution of Mip-NeRF360 dataset images varies across different works. Following the resolution setup in the 3D-GS work, we retrain some models on the Mip-NeRF360 dataset. Additionally, for works that did not report their storage usage, we report the results based on their released code.

Quality Comparisons. In Table 1, we present quantitative results comparing the rendering quality of our method with other approaches. From the table, we can see that our method achieves SOTA performance across all metrics on the Mip-NeRF360 [1] dataset. On the Tanks&Temples [24] dataset, our method also achieves the best SSIM and LPIPS metrics, which closely reflect human perception. In the Deep Blending [17] dataset, though our method does not achieve the highest score, it shows a notable improvement over the baseline. Additionally, our model variant with-

Table 2. **Efficiency comparison with former methods.**

| Dataset Method Metrics | Mip-NeRF360 | | Tanks&Temples | | Deep Blending | |
|-----------------------------|-------------|---------------|---------------|---------------|---------------|---------------|
| | FPS | Time | FPS | Time | FPS | Time |
| Octree-GS* | 119 | 29m55s | 126 | 23m8s | 151 | 34m38s |
| Scaffold-GS* | 103 | 23m53s | 137 | 15m37s | 141 | 19m40s |
| 3D-GS | 103 | 27m16s | 127 | 15m34s | 101 | 24m48s |
| AbsGS | 132 | 28m48s | 193 | 13m35s | 185 | 22m3s |
| Mini-Splatting-D | 74 | 34m42s | 75 | 27m39s | 100 | 30m37s |
| Pixel-GS* | 65 | 40m6s | 70 | 29m29s | 70 | 34m1s |
| Ours-Small (AbsGS) | 141 | 20m56s | 206 | 11m35s | 202 | 19m26s |
| Ours (AbsGS) | 100 | 29m24s | 150 | 16m29s | 153 | 23m33s |

out AbsGS [43] maintains similar performance to the full model, with only a slight reduction in LPIPS. Notably, our smaller model version achieves strong performance with reduced memory usage, showcasing the efficiency and scalability of our approach. In Fig. 5, we present qualitative comparisons between our method and several 3D-GS variants [23, 43, 50] across various scenes, including both indoor and outdoor settings. It is evident that our model captures finer details, as shown in the second, third, and fourth rows, constructs missing geometry more effectively (last row), and achieves more accurate geometry reconstruction (first row).

Efficiency Comparisons. We provide the computational costs of our method in comparison with other approaches in Table 2. It shows that our method involves a slight increase in training time while delivering much higher rendering quality than methods with lower rendering quality like 3D-GS [23] and AbsGS [43]. Our method is also significantly more efficient than other methods like Mini-Splatting-D [12], with comparable rendering quality. Notably, our small model provides the fastest FPS and shortest training time in all compared methods while maintaining high fidelity.

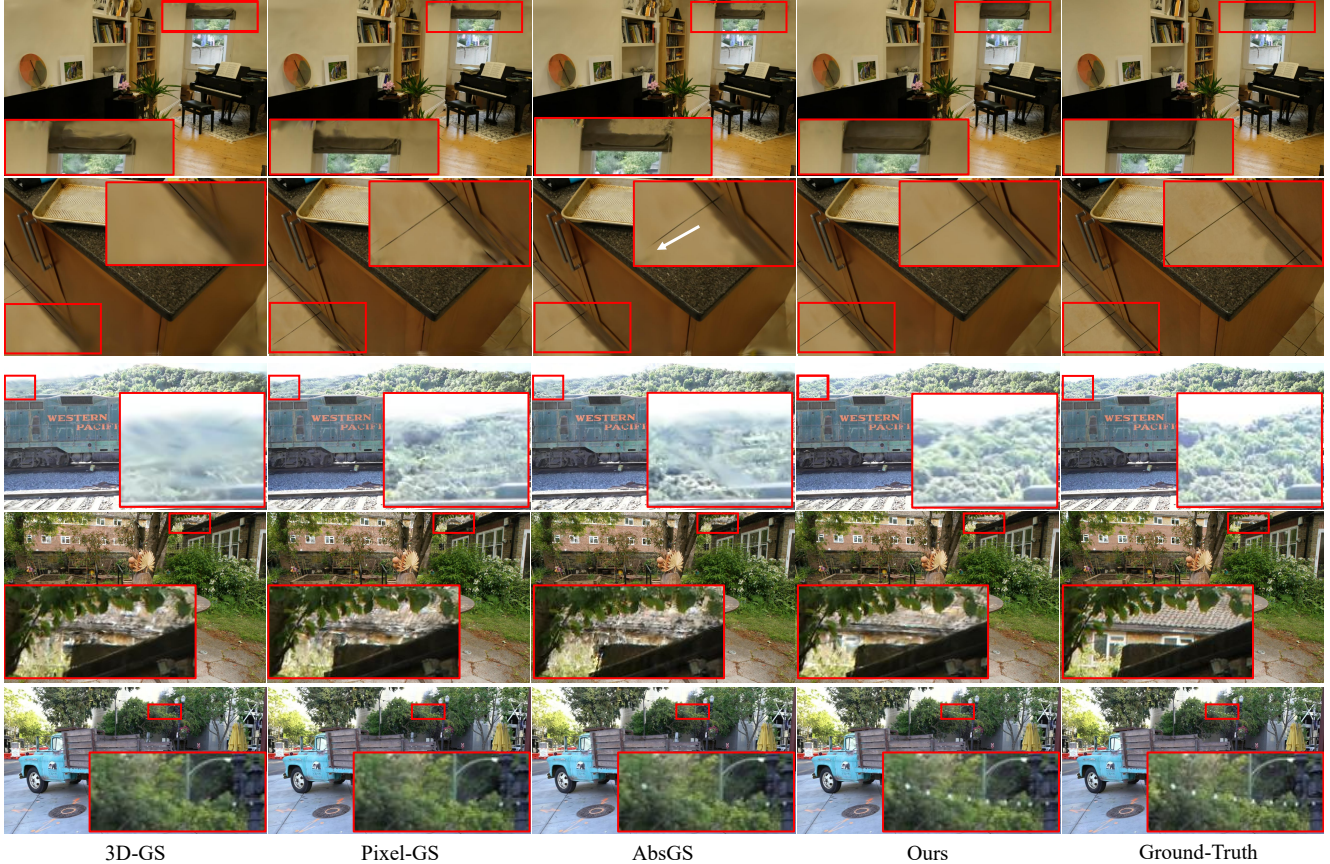


Figure 5. **Qualitative comparisons of ResGS with three 3D-GS variations on a variety of indoor and outdoor scenes.** Our approach captures more intrinsic details and acquires more complete geometry in complex scenes.

Table 3. **Analyzing residual split upon multiple 3D-GS variants.** The performance consistently increases on these pipelines, indicating that our residual split is a better densification operation. **3D-GS[†]** indicates a retrained version of 3D-GS [23] for better performance.

| Dataset Method Metrics | Mip-NeRF360 | | | | Tanks&Temples | | | | Deep Blending | | | |
|--|-----------------|-----------------|--------------------|--------|-----------------|-----------------|--------------------|--------|-----------------|-----------------|--------------------|--------|
| | PSNR \uparrow | SSIM \uparrow | LPIPS \downarrow | Mem | PSNR \uparrow | SSIM \uparrow | LPIPS \downarrow | Mem | PSNR \uparrow | SSIM \uparrow | LPIPS \downarrow | Mem |
| 3D-GS | 27.21 | 0.815 | 0.214 | 734MB | 23.14 | 0.841 | 0.183 | 411MB | 29.41 | 0.903 | 0.243 | 676MB |
| 3D-GS[†] | 27.38 | 0.813 | 0.215 | 821MB | 23.66 | 0.844 | 0.179 | 434MB | 29.48 | 0.900 | 0.247 | 663MB |
| 3D-GS + residual split | 27.44 | 0.813 | 0.216 | 586MB | 23.76 | 0.845 | 0.178 | 318MB | 29.75 | 0.902 | 0.240 | 546MB |
| AbsGS | 27.49 | 0.820 | 0.191 | 728MB | 23.73 | 0.853 | 0.162 | 304MB | 29.67 | 0.902 | 0.236 | 444MB |
| AbsGS + residual split | 27.71 | 0.827 | 0.185 | 712MB | 24.05 | 0.857 | 0.161 | 285MB | 29.68 | 0.905 | 0.234 | 421MB |
| Pixel-GS* | 27.52 | 0.822 | 0.191 | 1.32GB | 23.78 | 0.853 | 0.151 | 1.06GB | 28.91 | 0.892 | 0.250 | 1.09GB |
| Pixel-GS + residual split | 27.62 | 0.821 | 0.191 | 1.00GB | 24.05 | 0.856 | 0.148 | 754MB | 29.75 | 0.899 | 0.235 | 914MB |
| Mini-Splatting-D | 27.51 | 0.831 | 0.176 | 1.11GB | 23.23 | 0.853 | 0.140 | 1.01GB | 29.88 | 0.906 | 0.211 | 1.09GB |
| Mini-Splatting-D + residual split | 27.64 | 0.831 | 0.176 | 1.04GB | 23.49 | 0.853 | 0.140 | 967MB | 29.94 | 0.903 | 0.210 | 1.02GB |

4.3. Analysis

4.3.1. Residual Split

Compatibility. We analyze the compatibility of our novel densification operation by replacing split and clone in multiple 3D-GS variants [12, 23, 43, 50] with residual split. The hyperparameters are set the same as in the original pipelines. As Table 3 shows, our method leads to a notable increase in PSNR metrics across all pipelines, while for other metrics, some exhibit improvements, and others

remain approximately the same. Additionally, memory consumption is reduced after incorporating residual split compared to the original pipeline. This underscores our method’s ability to improve rendering quality and reduce redundancy, while also demonstrating its compatibility and potential for broader application across 3D-GS-oriented works as an effective alternative to split and clone.

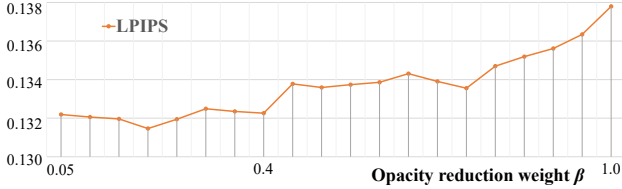


Figure 6. Impact of the opacity reduction weight β for residual split.

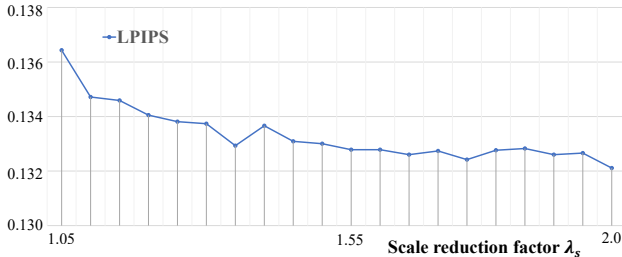


Figure 7. Impact of the scale reduction factor λ_s for residual split.

Table 4. Ablation Study on our pipeline. IP denotes image pyramid supervision, RS represents using residual split for densification, and VT indicates applying varying gradient threshold. Each component contributes to our method’s effectiveness.

| Dataset Method Metrics | Mip-NeRF360 | | | Deep Blending | | |
|-----------------------------|-----------------|-----------------|--------------------|-----------------|-----------------|--------------------|
| | PSNR \uparrow | SSIM \uparrow | LPIPS \downarrow | PSNR \uparrow | SSIM \uparrow | LPIPS \downarrow |
| Base | 27.41 | 0.817 | 0.189 | 29.60 | 0.899 | 0.240 |
| Base + RS | 27.66 | 0.825 | 0.183 | 29.68 | 0.900 | 0.233 |
| Base + IP | 27.54 | 0.823 | 0.182 | 29.05 | 0.896 | 0.245 |
| Base + RS + IP | 27.88 | 0.831 | 0.178 | 29.82 | 0.902 | 0.230 |
| Base + RS + IP + VT (full) | 28.00 | 0.833 | 0.174 | 29.91 | 0.902 | 0.227 |

Hyperparameter Sensitivities. Our residual split involves some hyperparameters: opacity reduction weight β and scale reduction factor λ_s . We conduct a corresponding sensitivity analysis on the Tanks&Temples [24] dataset while applying different $\beta \in [0.05, 1.0]$ and $\lambda_s \in [1.05, 2.0]$. All models are trained with similar storage. The LPIPS scores with different parameters are shown in Fig. 6 and 7. As they show, the LPIPS score remains relatively stable when $\beta < 0.4$ and $\lambda_s > 1.55$, indicating that our method is robust to hyperparameter variations, with only a 0.006 difference in LPIPS between the best and worst cases and a relatively broad range where rendering quality remains optimal.

4.3.2. Ablation Studies

To assess the effectiveness of our pipeline’s key modules, including residual split, image pyramid as supervision, and the varying gradient threshold, we conduct ablation studies on the Mip-NeRF360 [1] and Deep Blending [17] datasets. For the varying gradient threshold, we only conduct studies on its removal, as it is highly interdependent with the other

two modules. As the results in Table 4 shows, both residual split and image pyramid supervision individually boost the baseline’s performance on the Mip-NeRF360 dataset.

However, on Deep Blending, we observe a performance drop in **Base+IP**. This is because the dataset contains many weakly textured areas. As noted in Sec. 1, split and clone tend to fill such regions with an excessive number of small Gaussians. This makes them prone to overfitting the training views and lead to reduced performance on test views. The issue is amplified in the early iterations of a coarse-to-fine schedule, where only coarse scene information is available, making weakly textured areas even harder to resolve. As a result, these small Gaussians struggle to construct accurate geometry, leading to the performance drop observed in **Base+IP**.

Conversely, when using **RS**, weakly textured areas in early iterations are represented by only a few Gaussians, reducing overfitting. In later iterations, as finer information becomes available, **RS** progressively introduces more small Gaussians. As a result, **RS** benefits from progressive training, as evidenced by the improved performance of **Base+RS+IP** over **Base+RS**. This further proves **RS** is more effective than split and clone, especially in a coarse-to-fine schedule. Additionally, applying the varying gradient threshold (our full model) further boosts performance on both datasets, validating its effectiveness.

4.4. Discussions and Limitations

The above results demonstrate that our method significantly enhances rendering quality on the Mip-NeRF360 [1] and Tanks&Temples [24] datasets, achieving state-of-the-art performance. However, for the Deep Blending dataset [17], our method fails to achieve the best performance on every metric. While our approach implicitly constrains the number of Gaussians in weakly textured regions, which helps mitigate overfitting and improves quality, it does not include explicit regularization. This suggests an opportunity for further optimization in future work.

5. Conclusion

In this paper, we analyze the limitations of the current 3D-GS densification operation. To address these issues, we propose residual split, a residual empowered densification operation that adaptively handles both over-reconstruction and under-reconstruction. Additionally, we introduce ResGS, a coarse-to-fine 3D-GS pipeline to supplement residual split. Specifically, we use an image pyramid for supervision to gradually introduce fine details during Gaussian optimization. We also design a Gaussian selection scheme to further densify coarse Gaussians progressively. Our pipeline achieves SOTA rendering quality on several datasets while our residual split is highly compatible with other 3D-GS variants.

Acknowledgements

This work was supported by CAS Project for Young Scientists in Basic Research (YSBR-116).

References

- [1] Jonathan T. Barron, Ben Mildenhall, Matthew Tancik, Peter Hedman, Ricardo Martin-Brualla, and Pratul P. Srinivasan. Mip-nerf: A multiscale representation for anti-aliasing neural radiance fields. *IEEE/CVF International Conference on Computer Vision (ICCV)*, pages 5835–5844, 2021.
- [2] Jonathan T. Barron, Ben Mildenhall, Dor Verbin, Pratul P. Srinivasan, and Peter Hedman. Zip-nerf: Anti-aliased grid-based neural radiance fields. *IEEE/CVF International Conference on Computer Vision (ICCV)*, pages 19640–19648, 2023.
- [3] Yoshua Bengio, Jérôme Louradour, Ronan Collobert, and Jason Weston. Curriculum learning. *International Conference on Machine Learning (ICML)*, 2009.
- [4] M. Botsch, A. Hornung, M. Zwicker, and L. Kobbelt. High-quality surface splatting on today’s gpus. In *Proceedings Eurographics/IEEE VGTC Symposium Point-Based Graphics*, pages 17–141, 2005.
- [5] Samuel Rota Bulò, Lorenzo Porzi, and Peter Kotschieder. Revising densification in gaussian splatting. *ArXiv*, abs/2404.06109, 2024.
- [6] Eric R. Chan, Connor Z. Lin, Matthew A. Chan, Koki Nagano, Boxiao Pan, Shalini De Mello, Orazio Gallo, Leonidas Guibas, Jonathan Tremblay, Sameh Khamis, Tero Karras, and Gordon Wetzstein. Efficient geometry-aware 3D generative adversarial networks. In *IEEE/CVF Conference on Computer Vision and Pattern Recognition (CVPR)*, 2022.
- [7] Anpei Chen, Zexiang Xu, Fuqiang Zhao, Xiaoshuai Zhang, Fanbo Xiang, Jingyi Yu, and Hao Su. Mvsnerf: Fast generalizable radiance field reconstruction from multi-view stereo. *IEEE/CVF International Conference on Computer Vision (ICCV)*, pages 14104–14113, 2021.
- [8] Shuhong Chen, Kevin Zhang, Yichun Shi, Heng Wang, Yiheng Zhu, Guoxian Song, Sizhe An, Janus Kristjansson, X. Yang, and Matthias Zwicker. Panic-3d: Stylized single-view 3d reconstruction from portraits of anime characters. *IEEE/CVF Conference on Computer Vision and Pattern Recognition (CVPR)*, pages 21068–21077, 2023.
- [9] Shenchang Eric Chen and Lance R. Williams. View interpolation for image synthesis. *Seminal Graphics Papers: Pushing the Boundaries, Volume 2*, 1993.
- [10] Zilong Chen, Feng Wang, and Huaping Liu. Text-to-3d using gaussian splatting. *IEEE/CVF Conference on Computer Vision and Pattern Recognition (CVPR)*, pages 21401–21412, 2024.
- [11] Kai Cheng, Xiaoxiao Long, Kaizhi Yang, Yao Yao, Wei Yin, Yuexin Ma, Wenping Wang, and Xuejin Chen. Gaussianpro: 3d gaussian splatting with progressive propagation. *International Conference on Machine Learning (ICML)*, 2024.
- [12] Guangchi Fang and Bing Wang. Mini-splatting: Representing scenes with a constrained number of gaussians. In *European Conference on Computer Vision (ECCV)*, 2024.
- [13] Michael Goesele, Noah Snavely, Brian Curless, Hugues Hoppe, and Steven M. Seitz. Multi-view stereo for community photo collections. *IEEE 11th International Conference on Computer Vision (ICCV)*, pages 1–8, 2007.
- [14] Antoine Guédon and Vincent Lepetit. Sugar: Surface-aligned gaussian splatting for efficient 3d mesh reconstruction and high-quality mesh rendering. *IEEE/CVF Conference on Computer Vision and Pattern Recognition (CVPR)*, pages 5354–5363, 2024.
- [15] Zhiyang Guo, Wen gang Zhou, Li Li, Min Wang, and Houqiang Li. Motion-aware 3d gaussian splatting for efficient dynamic scene reconstruction. *IEEE Transactions on Circuits and Systems for Video Technology*, 35:3119–3133, 2024.
- [16] Kaiming He, X. Zhang, Shaoqing Ren, and Jian Sun. Spatial pyramid pooling in deep convolutional networks for visual recognition. *IEEE Transactions on Pattern Analysis and Machine Intelligence*, 37:1904–1916, 2014.
- [17] Peter Hedman, Julien Philip, True Price, Jan-Michael Frahm, George Drettakis, and Gabriel J. Brostow. Deep blending for free-viewpoint image-based rendering. *ACM Transactions on Graphics (TOG)*, 37:1 – 15, 2018.
- [18] Peter Hedman, Pratul P. Srinivasan, Ben Mildenhall, Jonathan T. Barron, and Paul E. Debevec. Baking neural radiance fields for real-time view synthesis. *IEEE/CVF International Conference on Computer Vision (ICCV)*, pages 5855–5864, 2021.
- [19] Tao Hu, Shu Liu, Yilun Chen, Tiancheng Shen, and Jiaya Jia. Efficientnerf efficient neural radiance fields. *IEEE/CVF Conference on Computer Vision and Pattern Recognition (CVPR)*, pages 12902–12911, 2022.
- [20] Binbin Huang, Zehao Yu, Anpei Chen, Andreas Geiger, and Shenghua Gao. 2d gaussian splatting for geometrically accurate radiance fields. In *SIGGRAPH Conference Papers*, 2024.
- [21] Ajay Jain, Matthew Tancik, and P. Abbeel. Putting nerf on a diet: Semantically consistent few-shot view synthesis. *IEEE/CVF International Conference on Computer Vision (ICCV)*, pages 5865–5874, 2021.
- [22] Tero Karras, Timo Aila, Samuli Laine, and Jaakko Lehtinen. Progressive growing of gans for improved quality, stability, and variation. In *International Conference on Learning Representations (ICLR)*, 2018.
- [23] Bernhard Kerbl, Georgios Kopanas, Thomas Leimkuehler, and George Drettakis. 3d gaussian splatting for real-time radiance field rendering. *ACM Transactions on Graphics (TOG)*, 42:1 – 14, 2023.
- [24] Arno Knapitsch, Jaesik Park, Qian-Yi Zhou, and Vladlen Koltun. Tanks and temples. *ACM Transactions on Graphics (TOG)*, 36:1 – 13, 2017.
- [25] Agelos Kratimenos, Jiahui Lei, and Kostas Daniilidis. Dynmf: Neural motion factorization for real-time dynamic view synthesis with 3d gaussian splatting. In *European Conference on Computer Vision (ECCV)*, 2024.
- [26] Minseop Kwak, Jiuhng Song, and Seung Wook Kim. Geconerf: Few-shot neural radiance fields via geometric consistency. *International Conference on Machine Learning (ICML)*, 2023.

- [27] Tao Lu, Mulin Yu, Linning Xu, Yuanbo Xiangli, Limin Wang, Dahua Lin, and Bo Dai. Scaffold-gs: Structured 3d gaussians for view-adaptive rendering. *IEEE/CVF Conference on Computer Vision and Pattern Recognition (CVPR)*, pages 20654–20664, 2024.
- [28] Hidenobu Matsuki, Riku Murai, Paul H.J. Kelly, and Andrew J. Davison. Gaussian splatting slam. *IEEE/CVF Conference on Computer Vision and Pattern Recognition (CVPR)*, pages 18039–18048, 2024.
- [29] Ben Mildenhall, Pratul P. Srinivasan, Matthew Tancik, Jonathan T. Barron, Ravi Ramamoorthi, and Ren Ng. Nerf: Representing scenes as neural radiance fields for view synthesis. In *European Conference on Computer Vision (ECCV)*, 2020.
- [30] Thomas Müller, Alex Evans, Christoph Schied, and Alexander Keller. Instant neural graphics primitives with a multiresolution hash encoding. *ACM Transactions on Graphics (TOG)*, 41:1 – 15, 2022.
- [31] Christian Reiser, Songyou Peng, Yiyi Liao, and Andreas Geiger. Kilonerf: Speeding up neural radiance fields with thousands of tiny mlps. *IEEE/CVF International Conference on Computer Vision (ICCV)*, pages 14315–14325, 2021.
- [32] Christian Reiser, Richard Szeliski, Dor Verbin, Pratul P. Srinivasan, Ben Mildenhall, Andreas Geiger, Jonathan T. Barron, and Peter Hedman. Merf: Memory-efficient radiance fields for real-time view synthesis in unbounded scenes. *ACM Transactions on Graphics (TOG)*, 42:1 – 12, 2023.
- [33] Kerui Ren, Lihan Jiang, Tao Lu, Mulin Yu, Linning Xu, Zhangkai Ni, and Bo Dai. Octree-gs: Towards consistent real-time rendering with lod-structured 3d gaussians. *IEEE transactions on pattern analysis and machine intelligence*, PP, 2024.
- [34] Andrei A. Rusu, Neil C. Rabinowitz, Guillaume Desjardins, Hubert Soyer, James Kirkpatrick, Koray Kavukcuoglu, Razvan Pascanu, and Raia Hadsell. Progressive neural networks. *ArXiv*, abs/1606.04671, 2016.
- [35] Johannes Lutz Schönberger and Jan-Michael Frahm. Structure-from-motion revisited. In *Conference on Computer Vision and Pattern Recognition (CVPR)*, 2016.
- [36] Pei Sun, Henrik Kretschmar, Xerxes Dotiwalla, Aurelien Chouard, Vijaysai Patnaik, Paul Tsui, James Guo, Yin Zhou, Yuning Chai, Benjamin Caine, Vijay Vasudevan, Wei Han, Jiquan Ngiam, Hang Zhao, Aleksei Timofeev, Scott M. Ettinger, Maxim Krivokon, Amy Gao, Aditya Joshi, Yu Zhang, Jonathon Shlens, Zhifeng Chen, and Dragomir Anguelov. Scalability in perception for autonomous driving: Waymo open dataset. *IEEE/CVF Conference on Computer Vision and Pattern Recognition (CVPR)*, pages 2443–2451, 2020.
- [37] Jiaxiang Tang, Jiawei Ren, Hang Zhou, Ziwei Liu, and Gang Zeng. Dreamgaussian: Generative gaussian splatting for efficient 3d content creation. In *International Conference on Learning Representations (ICLR)*, 2024.
- [38] Zhou Wang, Alan Conrad Bovik, Hamid R. Sheikh, and Eero P. Simoncelli. Image quality assessment: from error visibility to structural similarity. *IEEE Transactions on Image Processing*, 13:600–612, 2004.
- [39] Guanjun Wu, Taoran Yi, Jiemin Fang, Lingxi Xie, Xiaopeng Zhang, Wei Wei, Wenyu Liu, Qi Tian, and Xinggang Wang. 4d gaussian splatting for real-time dynamic scene rendering. *IEEE/CVF Conference on Computer Vision and Pattern Recognition (CVPR)*, pages 20310–20320, 2024.
- [40] Yuanbo Xiangli, Linning Xu, Xingang Pan, Nanxuan Zhao, Anyi Rao, Christian Theobalt, Bo Dai, and Dahua Lin. Bungeenerf: Progressive neural radiance field for extreme multi-scale scene rendering. In *European Conference on Computer Vision (ECCV)*, 2022.
- [41] Chi Yan, Delin Qu, Dong Wang, Dan Xu, Zhigang Wang, Bin Zhao, and Xuelong Li. Gs-slam: Dense visual slam with 3d gaussian splatting. *IEEE/CVF Conference on Computer Vision and Pattern Recognition (CVPR)*, pages 19595–19604, 2024.
- [42] Zeyu Yang, Hongye Yang, Zijie Pan, Xiatian Zhu, and Li Zhang. Real-time photorealistic dynamic scene representation and rendering with 4d gaussian splatting. In *International Conference on Learning Representations (ICLR)*, 2024.
- [43] Zongxin Ye, Wenyu Li, Sidun Liu, Peng Qiao, and Yong Dou. Absgs: Recovering fine details in 3d gaussian splatting. *Proceedings of the 32nd ACM International Conference on Multimedia*, 2024.
- [44] Taoran Yi, Jiemin Fang, Guanjun Wu, Lingxi Xie, Xiaopeng Zhang, Wenyu Liu, Qi Tian, and Xinggang Wang. Gaussiandreamer: Fast generation from text to 3d gaussians by bridging 2d and 3d diffusion models. In *IEEE/CVF Conference on Computer Vision and Pattern Recognition (CVPR)*, 2024.
- [45] Alex Yu, Sara Fridovich-Keil, Matthew Tancik, Qinhong Chen, Benjamin Recht, and Angjoo Kanazawa. Plenoxels: Radiance fields without neural networks. *IEEE/CVF Conference on Computer Vision and Pattern Recognition (CVPR)*, pages 5491–5500, 2022.
- [46] Zehao Yu, Anpei Chen, Binbin Huang, Torsten Sattler, and Andreas Geiger. Mip-splatting: Alias-free 3d gaussian splatting. *IEEE/CVF Conference on Computer Vision and Pattern Recognition (CVPR)*, pages 19447–19456, 2024.
- [47] Jingbo Zhang, Xiaoyu Li, Ziyu Wan, Can Wang, and Jing Liao. Fdnerf: Few-shot dynamic neural radiance fields for face reconstruction and expression editing. *SIGGRAPH Asia Conference Papers*, 2022.
- [48] Jiahui Zhang, Fangneng Zhan, Muyu Xu, Shijian Lu, and Eric P. Xing. Fregs: 3d gaussian splatting with progressive frequency regularization. *IEEE/CVF Conference on Computer Vision and Pattern Recognition (CVPR)*, pages 21424–21433, 2024.
- [49] Richard Zhang, Phillip Isola, Alexei A. Efros, Eli Shechtman, and Oliver Wang. The unreasonable effectiveness of deep features as a perceptual metric. *IEEE/CVF Conference on Computer Vision and Pattern Recognition*, pages 586–595, 2018.
- [50] Zheng Zhang, Wenbo Hu, Yixing Lao, Tong He, and Hengshuang Zhao. Pixel-gs: Density control with pixel-aware gradient for 3d gaussian splatting. In *European Conference on Computer Vision (ECCV)*, 2024.
- [51] Junyu Zhu, Hao Zhu, Qi Zhang, Fangfang Zhu, Zhan Ma, and Xun Cao. Pyramid nerf: Frequency guided fast radi-

ance field optimization. *International Journal of Computer Vision*, 131:2649–2664, 2023.

- [52] Zi-Xin Zou, Zhipeng Yu, Yuanchen Guo, Yangguang Li, Ding Liang, Yan-Pei Cao, and Song-Hai Zhang. Triplane meets gaussian splatting: Fast and generalizable single-view 3d reconstruction with transformers. *IEEE/CVF Conference on Computer Vision and Pattern Recognition (CVPR)*, pages 10324–10335, 2024.

ResGS: Residual Densification of 3D Gaussian for Efficient Detail Recovery

Supplementary Material

6. Additional Experiment Results

In this section, we provide additional experimental results of our work.

6.1. Evaluation on large-scale urban datasets

To evaluate the performance of our approach on large-scale urban datasets, we performed experiments using the Waymo [36] dataset and compared our results against GaussianPro [11]. The results are shown in the table below. It can be seen that our method achieves better results across all metrics.

Table 5. Results on the Waymo dataset compared with GaussianPro.

| Dataset | | Waymo | | | |
|--------------------|---------|-----------------|-----------------|--------------------|-------|
| Method | Metrics | PSNR \uparrow | SSIM \uparrow | LPIPS \downarrow | Mem. |
| GaussianPro | | 34.68 | 0.949 | 0.191 | 297MB |
| Ours | | 35.29 | 0.951 | 0.191 | 284MB |

6.2. Variance of PSNR on Deep Blending Dataset

A notable variance in the PSNR metrics of our method is observed on the Deep Blending [17] dataset. We tested our method on the Deep Blending dataset 10 times and reported the average performance and population standard deviation. The results are shown in Table 6. The table demonstrates that the PSNR scores on the Deep Blending dataset exhibit a notable variance. The underlying reason, as discussed in our limitations, is that our method does not address issues related to occlusion and overfitting, making the Deep Blending dataset particularly challenging for our approach. This highlights opportunities for future optimization and improvement. Furthermore, we report the average performance and population standard deviation over 10 runs for the other two datasets, Mip-NeRF360 [1] and Tanks&Temples [24], as presented in Table 7 and Table 8, respectively. The PSNR metrics for these two datasets do not show a notable variance, showcasing the robustness of our method in most scenarios.

Table 6. Average and standard deviation results of three metrics on the Deep Blending dataset.

| Dataset | | Deep Blending | | | | | |
|---------------------------|---------|-----------------|-------|-----------------|-------|--------------------|-------|
| Method | Metrics | PSNR \uparrow | | SSIM \uparrow | | LPIPS \downarrow | |
| | | Avg | Stdev | Avg | Stdev | Avg | Stdev |
| Ours-Small (AbsGS) | | 29.71 | 0.211 | 0.903 | 0.002 | 0.235 | 0.002 |
| Ours (3D-GS) | | 29.64 | 0.205 | 0.900 | 0.003 | 0.233 | 0.002 |
| Ours (AbsGS) | | 29.68 | 0.173 | 0.900 | 0.002 | 0.228 | 0.002 |

Table 7. Average and standard deviation results of three metrics on the Mip-NeRF360 dataset.

| Dataset | | Mip-NeRF360 | | | | | |
|---------------------------|---------|-----------------|-------|-----------------|-------|--------------------|-------|
| Method | Metrics | PSNR \uparrow | | SSIM \uparrow | | LPIPS \downarrow | |
| | | Avg | Stdev | Avg | Stdev | Avg | Stdev |
| Ours-Small (AbsGS) | | 27.93 | 0.010 | 0.830 | 0.001 | 0.191 | 0.001 |
| Ours (3D-GS) | | 27.99 | 0.011 | 0.831 | 0.001 | 0.187 | 0.001 |
| Ours (AbsGS) | | 27.99 | 0.011 | 0.833 | 0.001 | 0.174 | 0.001 |

Table 8. Average and standard deviation results of three metrics on the Tank&Temples dataset.

| Dataset | | Tank&Temples | | | | | |
|---------------------------|---------|-----------------|-------|-----------------|-------|--------------------|-------|
| Method | Metrics | PSNR \uparrow | | SSIM \uparrow | | LPIPS \downarrow | |
| | | Avg | Stdev | Avg | Stdev | Avg | Stdev |
| Ours-Small (AbsGS) | | 24.21 | 0.081 | 0.862 | 0.001 | 0.151 | 0.001 |
| Ours (3D-GS) | | 24.26 | 0.058 | 0.864 | 0.001 | 0.141 | 0.001 |
| Ours (AbsGS) | | 24.27 | 0.063 | 0.866 | 0.001 | 0.133 | 0.001 |

6.3. Further Analysis of Residual Split on 3D-GS

In our paper, we tested the compatibility of our residual split across multiple pipelines without modifying any hyper-parameters. Here, we present the results of applying residual split to 3D-GS [23] while adjusting the densification threshold τ to maintain the same storage size as 3D-GS, further demonstrating the capability of our method to enhance rendering quality. The results are shown in Table 9, showing that our method yields a further performance increase.

6.4. Results using random initialization

To assess the robustness of our method to random initialization, we conducted experiments using randomly initialized point clouds and compared our approach with other methods trained on the same random point clouds. The results are shown in Table 11. For the Mip-NeRF360 [1] and Tanks&Temples [24] datasets, our model shows a noticeable drop in quality compared to when initialized with SfM [35]. However, compared to other methods, it still achieves the best performance across all three metrics on Mip-NeRF360, and the highest SSIM and LPIPS on Tanks&Temples. As for Deep Blending [17], our method and others, excluding Scaffold-GS and Octree-GS, do not exhibit a significant performance drop. While we do not achieve the highest scores, our method remains competitive, ranking second across all metrics.

Table 9. Results of residual split upon 3D-GS with varied gradient threshold.

| Dataset | | Mip-NeRF360 | | | | Tanks&Temples | | | | Deep Blending | | | |
|-------------------------------|---------|-----------------|-----------------|--------------------|-------|-----------------|-----------------|--------------------|-------|-----------------|-----------------|--------------------|-------|
| Method | Metrics | PSNR \uparrow | SSIM \uparrow | LPIPS \downarrow | Mem | PSNR \uparrow | SSIM \uparrow | LPIPS \downarrow | Mem | PSNR \uparrow | SSIM \uparrow | LPIPS \downarrow | Mem |
| 3D-GS | | 27.21 | 0.815 | 0.214 | 734MB | 23.14 | 0.841 | 0.183 | 411MB | 29.41 | 0.903 | 0.243 | 676MB |
| 3D-GS + residual split | | 27.48 | 0.815 | 0.213 | 722MB | 23.85 | 0.846 | 0.174 | 374MB | 29.83 | 0.901 | 0.238 | 640MB |

Table 10. Results of our method without extended periodic opacity reduction. Here, **No EPOR** refers to our method trained without applying the extended periodic opacity reduction. **No EPOR + CT** refers to the model without the extended periodic opacity reduction but with an adjusted gradient threshold to ensure that the final storage size is approximately the same as our full model with extended periodic opacity reduction.

| Dataset | | Mip-NeRF360 | | | | Tanks&Temples | | | | Deep Blending | | | |
|----------------------------|---------|-----------------|-----------------|--------------------|-------|-----------------|-----------------|--------------------|-------|-----------------|-----------------|--------------------|-------|
| Method | Metrics | PSNR \uparrow | SSIM \uparrow | LPIPS \downarrow | Mem | PSNR \uparrow | SSIM \uparrow | LPIPS \downarrow | Mem | PSNR \uparrow | SSIM \uparrow | LPIPS \downarrow | Mem |
| Ours (No EPOR) | | 28.02 | 0.833 | 0.173 | 973MB | 24.32 | 0.867 | 0.130 | 591MB | 29.86 | 0.902 | 0.227 | 911MB |
| Ours (No EPOR + CT) | | 28.00 | 0.833 | 0.181 | 608MB | 24.35 | 0.866 | 0.139 | 380MB | 29.96 | 0.904 | 0.230 | 564MB |
| Ours (full) | | 28.00 | 0.833 | 0.174 | 698MB | 24.38 | 0.867 | 0.132 | 351MB | 29.91 | 0.902 | 0.227 | 586MB |

Table 11. Results using random initialized point clouds, compared with other methods.

| Dataset | | Mip-NeRF360 | | | | Tanks&Temples | | | | Deep Blending | | | |
|-------------------------|---------|-----------------|-----------------|--------------------|--------|-----------------|-----------------|--------------------|--------|-----------------|-----------------|--------------------|--------|
| Method | Metrics | PSNR \uparrow | SSIM \uparrow | LPIPS \downarrow | Mem. | PSNR \uparrow | SSIM \uparrow | LPIPS \downarrow | Mem. | PSNR \uparrow | SSIM \uparrow | LPIPS \downarrow | Mem. |
| Scaffold-GS | | 25.90 | 0.743 | 0.301 | 157MB | 22.00 | 0.768 | 0.282 | 51MB | 29.48 | 0.891 | 0.285 | 56MB |
| Octree-GS | | 25.70 | 0.739 | 0.292 | 190MB | 22.15 | 0.794 | 0.226 | 81MB | 28.29 | 0.873 | 0.300 | 92MB |
| 3D-GS | | 25.90 | 0.769 | 0.266 | 632MB | 21.19 | 0.777 | 0.241 | 339MB | 29.42 | 0.897 | 0.253 | 605MB |
| AbsGS | | 25.50 | 0.773 | 0.226 | 741MB | 20.89 | 0.786 | 0.211 | 304MB | 29.52 | 0.897 | 0.241 | 478MB |
| Mini-Splatting-D | | 25.18 | 0.792 | 0.207 | 1.10GB | 19.77 | 0.760 | 0.220 | 1.02GB | 29.76 | 0.901 | 0.212 | 1.09GB |
| Pixel-GS | | 26.23 | 0.792 | 0.221 | 1.14GB | 21.10 | 0.788 | 0.207 | 939MB | 28.76 | 0.889 | 0.256 | 1.04GB |
| Ours-Random | | 26.38 | 0.799 | 0.200 | 750MB | 22.02 | 0.815 | 0.178 | 282MB | 29.57 | 0.899 | 0.234 | 464MB |
| Ours-SFM | | 28.00 | 0.833 | 0.174 | 698MB | 24.38 | 0.867 | 0.132 | 351MB | 29.91 | 0.902 | 0.227 | 586MB |

6.5. Periodic Opacity Reduction

3D-GS [23] often encounters redundancy issues, which we categorize into two main causes: the first is the use of an excessive number of small-scale Gaussians to represent coarse areas, and the second is the overlap between Gaussians, resulting in redundant Gaussians that contribute minimally to the rendered image. Our residual split can solve the first issue but does not address the second. To tackle the second issue, as mentioned in our experiment settings, we implemented the periodic opacity reduction technique in [5, 43]. Specifically, the opacity of Gaussians is periodically reduced, causing the opacity of those that contribute little to the rendered image to diminish to a negligible value, allowing them to be effectively pruned. Additionally, we extended this operation to occur after the densification stage, discovering that it further reduces redundancy without compromising fidelity. Here, we present the experimental results of our method without extending the periodic opacity reduction operation, as shown in Table 10. From the table, we can observe that extending the periodic opacity reduction operation effectively reduces redundancy without compromising the fidelity of the rendered images. Furthermore, when the operation is not extended and the gradient threshold is adjusted to maintain storage approximately equal to

our full model, the rendering quality shows only a slight decrease in LPIPS metrics. This indicates that while extending the operation can enhance the performance of our method, its overall impact on the performance improvement is relatively minor.

6.6. Image Resolution of Mip-NeRF360 Dataset

In our paper, we mentioned that the image resolution on the Mip-NeRF360 [1] dataset varies across different works. 3D-GS [23] uses the provided “images_4”, the official downsampled 4 times images from the dataset, for outdoor scenes and “images_2” for indoor scenes. Most works [12, 43, 48] follow the 3D-GS setting, but Scaffold-GS [27], Octree-GS [33], Pixel-GS [50] uses different settings. Specifically, Scaffold-GS and Octree-GS downscale original images to 1.6K resolution, while Pixel-GS downscales original images by a factor of 4 for outdoor scenes and 2 for indoor scenes during the training process, instead of using the provided downsampled images. This discrepancy results in differences in experimental settings. To further demonstrate the performance of our method, we provide its results under the two different settings, as shown in Table 12 and 13. The tables show that our method prevails even under these alternate settings.

Table 13. Results on the Mip-NeRF360 dataset with same setting as Pixel-GS.

| Dataset | | Mip-NeRF360 | | |
|---------------------------|---------|-----------------|-----------------|--------------------|
| Method | Metrics | PSNR \uparrow | SSIM \uparrow | LPIPS \downarrow |
| Pixel-GS | | 27.88 | 0.834 | 0.176 |
| Ours-Small (AbsGS) | | 28.21 | 0.841 | 0.176 |
| Ours (3D-GS) | | 28.28 | 0.843 | 0.172 |
| Ours (AbsGS) | | 28.30 | 0.845 | 0.160 |

Table 12. Results on the Mip-NeRF360 dataset with same setting as Scaffold-GS and Octree-GS.

| Dataset | | Mip-NeRF360 | | |
|---------------------------|---------|-----------------|-----------------|--------------------|
| Method | Metrics | PSNR \uparrow | SSIM \uparrow | LPIPS \downarrow |
| Scaffold-GS | | 27.71 | 0.813 | 0.221 |
| Octree-GS | | 27.73 | 0.815 | 0.217 |
| Ours-Small (AbsGS) | | 28.04 | 0.831 | 0.191 |
| Ours (3D-GS) | | 28.10 | 0.832 | 0.187 |
| Ours (AbsGS) | | 28.14 | 0.834 | 0.174 |

6.7. Per Scene Results

We present the per-scene results of the used metrics in Table 14-19. For works that did not report per-scene results, we obtained and reported them using their released code. The works selected for comparison are mainly the same as in the paper: 3D-GS [23], Scaffold-GS [27], Octree-GS [33], AbsGS [43], Pixel-GS [50], Mini-Splatting-D [12], Plenoxels [45], Instant-NGP [30] and Mip-NeRF360 [1]. Note that we did not show the results of FreGS [48] since they did not report their per-scene results or release their code. Works retrained on the Mip-NeRF360 [1] are marked with a *.

Table 14. Per-scene PSNR metrics of Tank&Temples and Deep Blending dataset.

| Method | Scenes | Truck | Train | Dr Johnson | Playroom |
|---------------------------|--------|-------|-------|------------|----------|
| Plenoxels | | 23.22 | 18.93 | 23.14 | 22.98 |
| Instant-NGP | | 23.38 | 20.46 | 28.26 | 21.67 |
| Mip-NeRF360 | | 24.91 | 19.52 | 29.14 | 29.66 |
| Scaffold-GS | | 25.77 | 22.15 | 29.80 | 30.62 |
| Octree-GS | | 26.27 | 22.77 | 29.87 | 30.95 |
| 3D-GS | | 25.19 | 21.10 | 28.77 | 30.04 |
| AbsGS | | 25.74 | 21.72 | 29.20 | 30.14 |
| Pixel-GS | | 25.49 | 22.13 | 28.02 | 29.79 |
| Mini-Splatting-D | | 25.43 | 21.04 | 29.32 | 30.43 |
| Ours-Small (AbsGS) | | 26.07 | 22.40 | 29.64 | 30.38 |
| Ours (3D-GS) | | 26.08 | 22.65 | 29.54 | 30.32 |
| Ours (AbsGS) | | 26.14 | 22.61 | 29.51 | 30.32 |

Table 15. Per-scene SSIM metrics of Tank&Temples and Deep Blending dataset.

| Method | Scenes | Truck | Train | Dr Johnson | Playroom |
|---------------------------|--------|-------|-------|------------|----------|
| Plenoxels | | 0.774 | 0.663 | 0.787 | 0.802 |
| Instant-NGP | | 0.800 | 0.689 | 0.854 | 0.779 |
| Mip-NeRF360 | | 0.857 | 0.660 | 0.901 | 0.900 |
| Scaffold-GS | | 0.883 | 0.822 | 0.907 | 0.904 |
| Octree-GS | | 0.896 | 0.835 | 0.912 | 0.914 |
| 3D-GS | | 0.879 | 0.802 | 0.899 | 0.906 |
| AbsGS | | 0.888 | 0.818 | 0.898 | 0.907 |
| Pixel-GS | | 0.883 | 0.823 | 0.885 | 0.899 |
| Mini-Splatting-D | | 0.890 | 0.817 | 0.905 | 0.908 |
| Ours-Small (AbsGS) | | 0.889 | 0.834 | 0.905 | 0.907 |
| Ours (3D-GS) | | 0.890 | 0.840 | 0.901 | 0.905 |
| Ours (AbsGS) | | 0.893 | 0.841 | 0.900 | 0.905 |

Table 16. Per-scene LPIPS metrics of Tank&Temples and Deep Blending dataset.

| Method | Scenes | Truck | Train | Dr Johnson | Playroom |
|---------------------------|--------|-------|-------|------------|----------|
| Plenoxels | | 0.335 | 0.422 | 0.521 | 0.499 |
| Instant-NGP | | 0.249 | 0.360 | 0.352 | 0.428 |
| Mip-NeRF360 | | 0.159 | 0.354 | 0.237 | 0.252 |
| Scaffold-GS | | 0.147 | 0.206 | 0.250 | 0.258 |
| Octree-GS | | 0.118 | 0.198 | 0.231 | 0.244 |
| 3D-GS | | 0.148 | 0.218 | 0.244 | 0.241 |
| AbsGS | | 0.132 | 0.193 | 0.241 | 0.233 |
| Pixel-GS | | 0.122 | 0.180 | 0.258 | 0.243 |
| Mini-Splatting-D | | 0.100 | 0.181 | 0.218 | 0.204 |
| Ours-Small (AbsGS) | | 0.124 | 0.177 | 0.233 | 0.235 |
| Ours (3D-GS) | | 0.118 | 0.164 | 0.232 | 0.231 |
| Ours (AbsGS) | | 0.106 | 0.159 | 0.231 | 0.223 |

Table 17. Per-scene PSNR metrics of Mip-NeRF360 dataset.

| Method | Scenes | bicycle | flowers | garden | stump | treehill | room | counter | kitchen | bonsai |
|---------------------------|--------|---------|---------|--------|-------|----------|-------|---------|---------|--------|
| Plenoxels | | 21.91 | 20.10 | 23.49 | 20.66 | 22.25 | 27.59 | 23.62 | 23.42 | 24.67 |
| Instant-NGP | | 22.17 | 20.65 | 25.07 | 23.47 | 22.37 | 29.69 | 26.69 | 29.48 | 30.69 |
| Mip-NeRF360 | | 24.31 | 21.65 | 26.88 | 26.18 | 22.93 | 31.47 | 29.45 | 31.99 | 33.40 |
| Scaffold-GS* | | 25.07 | 21.36 | 27.35 | 26.64 | 22.93 | 32.04 | 29.50 | 31.63 | 32.71 |
| Octree-GS* | | 25.05 | 21.33 | 27.58 | 26.41 | 22.81 | 32.09 | 29.48 | 30.89 | 31.71 |
| 3D-GS | | 25.25 | 21.52 | 27.41 | 26.55 | 22.49 | 30.63 | 28.70 | 30.32 | 31.98 |
| AbsGS | | 25.29 | 21.35 | 27.48 | 26.71 | 21.99 | 31.61 | 29.03 | 31.62 | 32.32 |
| Pixel-GS* | | 25.21 | 21.49 | 27.42 | 26.84 | 22.09 | 31.45 | 29.05 | 31.65 | 32.53 |
| Mini-Splatting-D | | 25.55 | 21.50 | 27.67 | 27.11 | 22.13 | 31.41 | 28.72 | 31.75 | 31.72 |
| Ours-Small (AbsGS) | | 25.62 | 21.80 | 27.72 | 27.27 | 22.90 | 32.41 | 29.32 | 31.95 | 32.48 |
| Ours (3D-GS) | | 25.55 | 22.07 | 27.71 | 27.12 | 22.82 | 32.48 | 29.41 | 32.09 | 32.74 |
| Ours (AbsGS) | | 25.62 | 21.78 | 27.82 | 27.19 | 22.57 | 32.51 | 29.50 | 32.26 | 32.78 |

Table 18. Per-scene SSIM metrics of Mip-NeRF360 dataset.

| Method | Scenes | bicycle | flowers | garden | stump | treehill | room | counter | kitchen | bonsai |
|---------------------------|--------|---------|---------|--------|-------|----------|--------|---------|---------|--------|
| Plenoxels | | 0.496 | 0.431 | 0.6063 | 0.523 | 0.509 | 0.8417 | 0.759 | 0.648 | 0.814 |
| Instant-NGP | | 0.512 | 0.486 | 0.701 | 0.594 | 0.542 | 0.871 | 0.817 | 0.858 | 0.906 |
| Mip-NeRF360 | | 0.685 | 0.584 | 0.809 | 0.745 | 0.631 | 0.910 | 0.892 | 0.917 | 0.938 |
| Scaffold-GS* | | 0.755 | 0.590 | 0.858 | 0.765 | 0.639 | 0.923 | 0.910 | 0.926 | 0.943 |
| Octree-GS* | | 0.759 | 0.597 | 0.864 | 0.763 | 0.643 | 0.924 | 0.907 | 0.916 | 0.930 |
| 3D-GS | | 0.771 | 0.605 | 0.868 | 0.775 | 0.638 | 0.914 | 0.905 | 0.922 | 0.938 |
| AbsGS | | 0.783 | 0.623 | 0.871 | 0.780 | 0.617 | 0.925 | 0.911 | 0.929 | 0.945 |
| Pixel-GS* | | 0.775 | 0.633 | 0.867 | 0.784 | 0.630 | 0.920 | 0.911 | 0.929 | 0.944 |
| Mini-Splatting-D | | 0.798 | 0.642 | 0.878 | 0.804 | 0.640 | 0.928 | 0.913 | 0.934 | 0.946 |
| Ours-Small (AbsGS) | | 0.792 | 0.634 | 0.872 | 0.802 | 0.652 | 0.929 | 0.914 | 0.932 | 0.945 |
| Ours (3D-GS) | | 0.790 | 0.639 | 0.874 | 0.800 | 0.650 | 0.929 | 0.916 | 0.934 | 0.947 |
| Ours (AbsGS) | | 0.797 | 0.647 | 0.876 | 0.804 | 0.645 | 0.931 | 0.918 | 0.934 | 0.948 |

Table 19. Per-scene LPIPS metrics of Mip-NeRF360 dataset.

| Method | Scenes | bicycle | flowers | garden | stump | treehill | room | counter | kitchen | bonsai |
|---------------------------|--------|---------|---------|--------|-------|----------|--------|---------|---------|--------|
| Plenoxels | | 0.506 | 0.521 | 0.3864 | 0.503 | 0.540 | 0.4186 | 0.441 | 0.447 | 0.398 |
| Instant-NGP | | 0.446 | 0.441 | 0.257 | 0.421 | 0.450 | 0.261 | 0.306 | 0.195 | 0.205 |
| Mip-NeRF360 | | 0.301 | 0.344 | 0.170 | 0.261 | 0.339 | 0.211 | 0.204 | 0.127 | 0.176 |
| Scaffold-GS* | | 0.233 | 0.352 | 0.120 | 0.236 | 0.331 | 0.216 | 0.203 | 0.130 | 0.207 |
| Octree-GS* | | 0.225 | 0.340 | 0.108 | 0.233 | 0.310 | 0.203 | 0.202 | 0.141 | 0.219 |
| 3D-GS | | 0.205 | 0.336 | 0.103 | 0.210 | 0.317 | 0.220 | 0.204 | 0.129 | 0.205 |
| AbsGS | | 0.171 | 0.270 | 0.100 | 0.195 | 0.278 | 0.200 | 0.189 | 0.121 | 0.190 |
| Pixel-GS* | | 0.182 | 0.263 | 0.100 | 0.186 | 0.280 | 0.213 | 0.185 | 0.120 | 0.193 |
| Mini-Splatting-D | | 0.158 | 0.255 | 0.090 | 0.169 | 0.262 | 0.190 | 0.172 | 0.114 | 0.175 |
| Ours-Small (AbsGS) | | 0.175 | 0.290 | 0.099 | 0.188 | 0.279 | 0.196 | 0.184 | 0.117 | 0.189 |
| Ours (3D-GS) | | 0.168 | 0.295 | 0.092 | 0.179 | 0.280 | 0.192 | 0.177 | 0.114 | 0.185 |
| Ours (AbsGS) | | 0.156 | 0.251 | 0.089 | 0.170 | 0.250 | 0.187 | 0.172 | 0.112 | 0.179 |